Wavelength selection of vortex ripples in an oscillating cylinder: The effect of curvature and background rotation

M. Duran-Matute,[1,*] M. D. van Gorp,[2,3] and G. J. F. van Heijst[1]

[1]*Fluid Dynamics Laboratory, Department of Applied Physics and J.M. Burgers Centre for Fluid Dynamics,*
Eindhoven University of Technology, P.O. Box 513, 5600MB Eindhoven, The Netherlands
[2]*Fluid Dynamics Laboratory, Department of Applied Physics, Eindhoven University of Technology,*
P.O. Box 513, 5600MB Eindhoven, The Netherlands
[3]*Re/genT, Lagedijk 22, 5705BZ Helmond, The Netherlands*

We present results of laboratory experiments on the formation, evolution, and wavelength selection of vortex ripples. These ripples formed on a sediment bed at the bottom of a water-filled oscillating cylindrical tank mounted on top of a rotating table. The table is made to oscillate sinusoidally in time, while a constant background rotation was added for some experiments. The changes in bed thickness are measured using a light attenuation technique. It was found that the wavelength normalized with the excursion length depends on both a Reynolds number and the Strouhal number. This differs from straight or annular geometries where the wavelength is proportional to the excursion length. The flow in an oscillating cylinder has the peculiarity that it develops a secondary flow in the radial direction that depends on the excursion length. The effect of this secondary circulation is evident in the radial transport for small values of the Strouhal number or in the orientation of the ripples for strong enough background rotation. Additionally, ripples in an oscillating cylinder present a rich dynamic behavior where the number of ripples can oscillate even with constant forcing parameters.

I. INTRODUCTION

The scientific study of sand ripples started over a century ago with the early work by de Candolle [1] and Darwin [2] motivated mainly by the ripples formed under the action of gravity water waves close to the coast. However, research is still ongoing due to the complex interplay between the solid and liquid phases, and the resulting complex dependence of the ripple properties on several parameters (see, e.g., Ref. [3]). Determining this dependence and accurately predicting the geometrical properties of ripples is of particular importance to determine the effect of the ripples on waves, currents, and sediment transport in coastal areas [4].

Ripples are initially formed by the destabilization of the bed by the oscillating flow and the formation of recirculating cells that transport sand from the troughs to the crests. When the ripples are large enough, the flow separates behind the ripple's crest, forming a vortex with a horizontal axis. These ripples are hence known as *vortex ripples*. The vortex keeps on eroding the troughs and transporting sediment to the crests until a final ripple geometry is reached.

The dependence of the ripple geometry (wavelength and height) as a function of several parameters has been studied extensively both in laboratory experiments and in field measurements (a detailed overview is given in Ref. [5]). Efforts are being made to numerically reproduce the dynamics of vortex ripples [6–8], but further improvements and more computational power are still needed to realistically reproduce the long-term evolution of many ripples simultaneously. Therefore, laboratory experiments are still the only option to study the behavior of vortex ripples in well-controlled situations. Mostly, these experiments are carried out in straight oscillatory flow tunnels (e.g., Refs. [9–12]) and wave flumes (e.g., Refs. [13,14]). However, some experiments have also been carried out in oscillating cylinders [1,15,16] and annular channels [17–19]. These geometries present several advantages such as a compact size, ease of control, and the absence of end-wall effects.

Within a limited region of the parameters space (known as the orbital ripple regime [20]), the ripple wavelength is proportional to the excursion length of the water [9,14,18,21,22], which means that it is independent of the sediment properties as found in the pioneering work by Bagnold and Taylor [23]. In particular, a proportionality value of about 2/3 between the ripple wavelength and the excursion length of the water has been recurrently found in different geometries [9,18,21,22]. This value is attributed to the resonance between the rippled bed and the vortices shed from the ripple crests [24,25]. Additionally, Stegner and Wesfreid [18] found a strong hysteresis in an annular geometry: the wavelength would grow when the excursion length increases, but it would not diminish if the excursion length decreases. Subsequently, Testik *et al.* [13] did not find such a hysteresis for changing wave conditions in a wave flume.

In an oscillating cylinder, radial ripples form outside a critical radius [1,16] where the flow is strong enough to move the sediment grains. Curvature and background rotation are well known to force secondary flows—with a radial velocity component at the bottom (see, e.g., Ref. [26]). It is then

surprising that previous work on vortex ripples in oscillating cylinders has mainly found similarities with the formation and geometry of ripples in straight geometries. For example, Rousseaux *et al.* [16] did not find a net radially outward sediment transport as would be expected from the secondary motion, and they concluded that the excursion length and the wavelength of the radial ripples must be proportional to each other since they are both proportional to the radial position.

However, as it will be shown in the present paper, the strength of the secondary flow increases with the excursion length. It is then unclear if the previous conclusion about the dependence of the ripple wavelength to the forcing parameters is only valid within a limited region of the parameter space. Actually, it should be expected that the dependence of both the flow and the sediment response to the excursion length results in a more complex dependence of the ripple wavelength to the forcing parameters. To clarify these points, we presents results of laboratory experiments where we systematically study the effects of the secondary flow due to curvature and background rotation on the vortex ripples formed in a sediment bed at the bottom of an oscillating fluid-filled cylindrical tank. In the experiments, we varied both the amplitude and the frequency of the oscillation within a broad range of values, and we used two different sorts of artificial sediment. In this way, we were able to explore a large region of the parameter space to unravel the complex interplay between the flow and the sediment.

The rest of the paper is organized as follows. In Sec. II, we present the necessary theoretical background including the description of the problem, the definition of the governing parameters, and a semi-analytical description of the flow over an oscillating infinite disk with and without additional background rotation. The experimental setup and the measurement technique are then described in Sec. III. Section IV presents the results of the experiments on the formation of the ripples, the dependence of the wavelength on the forcing parameters, and the stability of the patterns observed. Finally, the conclusions are outlined in Sec. V.

II. DESCRIPTION OF THE PROBLEM

Laboratory experiments are used to study the evolution of a sediment bed under an oscillating swirling flow inside a cylinder of radius R. For simplicity, the swirling flow is created by oscillating the fluid-filled tank, thus creating a relative motion between the fluid and the particle bed. The tank's angular velocity $\Omega(t)$ is given by

$$\Omega(t) = \Omega_o \sin(\omega t) + \Omega_c, \tag{1}$$

where Ω_o is the angular velocity amplitude of the oscillation, ω is the angular frequency of the oscillation, and Ω_c is a constant background rotation superimposed to the main oscillating motion. For most experiments described here, $\Omega_c = 0$. The excursion length L of the fluid high above the bed is then given by

$$L = \frac{2\Omega_o r}{\omega}, \tag{2}$$

with r the radial distance from the center of the cylinder.

A. Parameters of the problem

For the flow, the relevant nondimensional parameters are the Strouhal number,

$$\text{Sr} = \frac{\omega}{\Omega_o}, \tag{3}$$

representing the ratio of the local acceleration to the convective acceleration (the acceleration due to the movement of the fluid particle to a different part of the flow field); the Reynolds number,

$$\text{Re} = \frac{R^2 \Omega_o}{\nu}, \tag{4}$$

representing the ratio of the convective acceleration to viscous drag, and the Rossby number

$$\text{Ro} = \frac{\Omega_o}{\Omega_c}, \tag{5}$$

representing the ratio of the convective acceleration to the Coriolis acceleration. Note that the Strouhal number Sr is also equivalent to the ratio of the radial position r to half the excursion length: $\text{Sr} = 2r/L$. In other words, the Strouhal number can be seen as a measure of the excursion length relative to the radius. Beside the parameters already defined, one can define a Reynolds number based on the excursion length Eq. (2) at $r = R$ as

$$\text{Re}_L = 2\frac{\text{Re}}{\text{Sr}} = 2\frac{R^2 \Omega_o^2}{\nu \omega}, \tag{6}$$

which is associated to the strength of the ripple vortex.

The interaction between the flow and the sediment can be characterized by the Shields parameter defined as

$$\theta = \frac{\tau_b}{(\rho_p/\rho_l - 1)gd}, \tag{7}$$

where τ_b is the shear stress at the bottom, ρ_p is the density of the particles, ρ_l is the density of the fluid, and $g = 9.81 \text{ m s}^{-2}$ is the gravitational acceleration. The sediment is characterized by its critical Shields parameter θ_{cr}, which is given by the value of θ that is needed to initiate the motion of sediment particles. Related to the Shields parameter, it is also useful to define the bed-shear stress parameter:

$$T = \frac{\theta - \theta_{\text{cr}}}{\theta_{\text{cr}}} \tag{8}$$

to quantify the difference between the applied shear stress and the critical shear stress [27].

Another commonly used option to characterize the interaction between the flow and the sediment is the mobility parameter:

$$\Psi = \frac{\Omega_o^2 R^2}{(\rho_p/\rho_l - 1)gd}, \tag{9}$$

where the typical velocity scale is the maximum velocity at $r = R$: $\Omega_o R$. In fact, Nielsen [28] proposed a relationship between the ripple wavelength and the mobility parameter. However, in an oscillating cylinder, the mobility parameter based on the local velocity—as defined in a straight geometry— varies from zero at $r = 0$ to Ψ at $r = R$.

B. The boundary layer over an oscillating disk

As a first step to understand the flow over the sediment bed, we study the flow above an infinitely large oscillating disk using a similar approach as Owen and Rogers [26] but including time dependence. For convenience, we use cylindrical coordinates (r, θ, z). The angular velocity of the disk $\Omega(t)$ is given by Eq. (1), and the flow above rotates with the whole system with $v_\theta = r\Omega_c$ as $z \to \infty$. Furthermore, we assume that the flow is axisymmetric ($\partial/\partial\theta = 0$) and that the azimuthal and radial velocity components are proportional to r. The radial pressure gradient can be written as

$$\frac{1}{\rho}\frac{\partial p}{\partial r} = r\Omega_c^2 \qquad (10)$$

[26].

We define the nondimensional variables (denoted by a prime):

$$u'_r = \frac{u_r}{r\Omega_o}, \quad u'_\theta = \frac{u_\theta}{r\Omega_o}, \quad u'_z = \frac{u_z}{\delta^*\Omega_o}, \quad t' = \omega t,$$

$$z' = \sqrt{\frac{\Omega_o}{\nu}}z, \quad p' = \frac{p}{\rho\nu\Omega_o}.$$

The Navier-Stokes equations and the continuity equation for the flow can then be written in nondimensional form as

$$\text{Sr}\frac{\partial u'_r}{\partial t'} + u'^2_r + u'_z\frac{\partial u'_r}{\partial z'} - u'^2_\phi + \text{Ro}^{-2} = \frac{\partial^2 u'_r}{\partial z'^2}, \qquad (11a)$$

$$\text{Sr}\frac{\partial u'_\phi}{\partial t'} + 2u'_r u'_\phi + u'_z\frac{\partial u'_\phi}{\partial z'} = \frac{\partial^2 u'_\phi}{\partial z'^2}, \qquad (11b)$$

$$\text{Sr}\frac{\partial u'_z}{\partial t'} + u'_r u'_z + u'_z\frac{\partial u'_z}{\partial z'} = -\frac{\partial p'}{\partial z'} + \frac{\partial^2 u'_z}{\partial z'^2}, \qquad (11c)$$

$$\frac{\partial u'_z}{\partial z'} = -2u'_r, \qquad (11d)$$

where the term Ro^{-2} represents the radial pressure gradient. Already from these equations, it can be seen that the Strouhal number (and hence, the excursion length) is one of the parameters governing the flow.

Equations (11) were solved numerically for different Sr and Ro values. However, it can be easily shown that in the limit $\text{Sr} \to \infty$ and $\text{Ro} \to \infty$, the equations describing the classical Stokes boundary layer (equivalent to those in a straight channel) are recovered. In the limit $\text{Sr} = 0$, we recover well known stationary solutions: the von Kármán flow (with $\text{Ro} \to \infty$) and the Ekman boundary layer flow (with $|\text{Ro}| \ll 1$).

Since we are interested in the effect of the flow on the bed, we will focus here on the shear stress $\boldsymbol{\tau}$ at the bottom of the flow obtained by solving Eq. (11). The nondimensional shear stress $\boldsymbol{\tau}'$ is defined as $\boldsymbol{\tau}' = \boldsymbol{\tau}/(\rho r \nu^{1/2}\Omega_o^{3/2})$.

Figure 1 shows the trace of $\boldsymbol{\tau}'$ for two cases: ($\text{Sr} = 0.5848$, $\text{Ro} = \infty$) and ($\text{Sr} = 0.5848$, $\text{Ro} = 1.25$). For the case without background rotation and $\text{Sr} = 0.5848$, the shear stress in the azimuthal direction oscillates back and forth, while there is a pulsating radially outward shear stress with a phase lag. For the case with background rotation and $\text{Sr} = 0.5848$, the flow
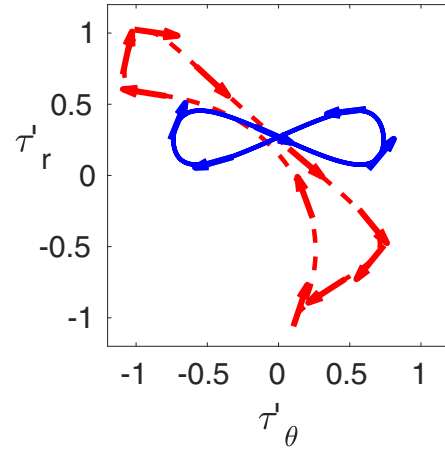

FIG. 1. Trace of the dimensionless shear stress (τ'_r vs. τ'_θ) at the bottom for an oscillating disk with $\text{Sr} = 0.5848$ and $\text{Ro} = \infty$ (solid line) and $\text{Sr} = 0.5848$, $\text{Ro} = 1.25$ (dashed line). The arrows indicate the direction of time.

oscillates in both the azimuthal and radial direction, and a clear asymmetry between the cyclonic and anticyclonic half of the oscillation can be observed. The solution to Eq. (11) does not exist for all values of Ro. This was observed already for the stationary case for $\text{Ro} < -0.2$ (i.e., for large anticyclonic flow velocities) [26]. It was observed by performing numerical simulations solving the two-dimensional axisymmetric Navier-Stokes equations in cylindrical coordinates that the assumption that $v_r \propto r$ does not hold in such a case. Instead, v_r can be positive for certain values of r and negative for some others with a stagnation point in between.

Figure 2 shows the amplitude of the shear stress as a function of the Strouhal number for solutions to Eq. (11) without background rotation. The amplitude of the total shear stress is compared to the total shear stress for a von Karman flow (i.e., constantly rotating disk), which is given by $|\tau'| = 0.8$ and for a Stokes boundary layer (i.e., boundary layer under
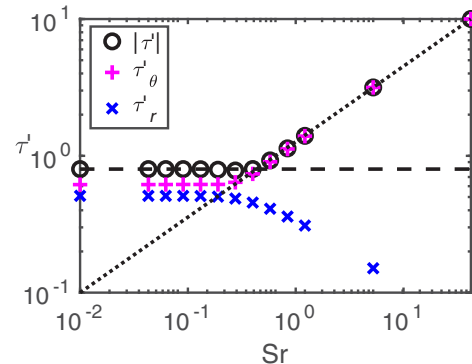

FIG. 2. Magnitude of the shear stress above an oscillating disk as a function of the Strouhal number (Sr) without background rotation. The symbols represent the amplitude of the total shear stress $|\tau'|$ ($\circ$), the amplitude of the shear stress in the azimuthal direction τ_θ ($+$), and the amplitude of the shear stress in the radial direction τ_r ($\times$). The dashed line represents the value of the total shear stress for a von Karman flow, and the dotted line represents the shear stress for a Stokes boundary layer.
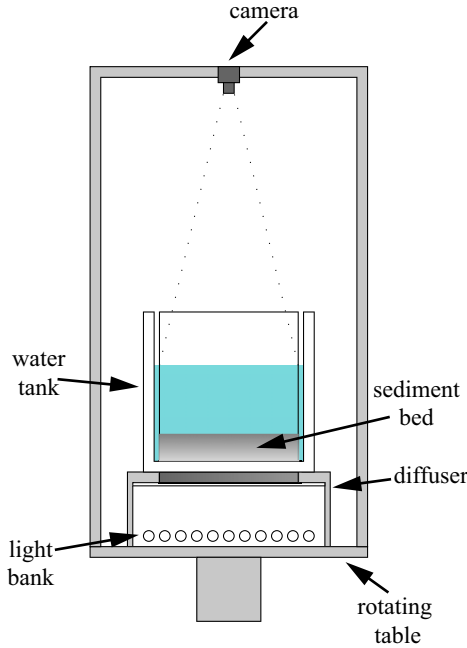
FIG. 3. Schematic side view of the experimental setup.

TABLE I. Properties of the different types of sediment-fluid combinations used. Herein, d is a typical length scale of the particles: the radius for the PS spherical particles, and the radius or length for the PMMA particles since they are about equal; n_p is the refractive index of the particles; n_l is the refractive index of the fluid; ρ_p is the volumetric mass density of the particles; ρ_l is the volumetric mass density of the fluid; g' is the reduced gravity for the particles in the fluid; ν is the kinematic viscosity of the fluid; and $\bar{z}$ is the sediment layer thickness at the start of the experiment.

Particle type	PMMA	PS
Water type	Salt	Fresh
Particle shape	Cylindrical	Spherical
d	2–3 mm	0.58 mm
n_p	1.4914	1.6
n_l	1.3576	1.3330
ρ_p	1.18 g/cm^3	1.05 g/cm^3
ρ_l	1.10 g/cm^3	0.998 g/cm^3
g'	$0.0727g$	$0.0521g$
ν	1.12×10^{-6} m^2/s	10^{-6} m^2/s
$\bar{z}$	5 cm	2 cm

an oscillating flow in a straight geometry) which is given by $|\tau'| = (\omega/\Omega_0)^{1/2} = \mathrm{Sr}^{1/2}$. The intersection of these two solutions indicates a transition in the behavior of the boundary layer: For $\mathrm{Sr} < 0.8^2 = 0.64$, the boundary layer tends toward a von Karman–type flow, with a radial shear stress of the same order of magnitude than the azimuthal shear stress; for $\mathrm{Sr} > 0.64$, the flow tends toward a Stokes boundary layer flow and the radial shear stress becomes negligible with increasing Sr values. In other words, the influence of the domain's curvature becomes negligible for large Sr values when the excursion length of the oscillation is much smaller than the radius.

In the remainder of the paper, we will show how these properties of the flow translate into differences in the morphological evolution of a sediment bed placed under it. Note that Rousseaux *et al.* [16] only performed experiments with Sr values one order of magnitude larger than the critical value $\mathrm{Sr} = 0.64$, and hence, they might not have observed the influence of the curvature of the domain. In the current paper, the experiments presented were carried out with Sr values spanning across the critical value $\mathrm{Sr} = 0.64$.

III. METHODS

A. Experimental setup and procedure

A transparent cylindrical perspex tank with an inner diameter of 49 cm was placed on top of a rotating table. The tank was filled with water up to a depth of 30 cm, and a flat layer with thickness $\bar{z}$ of translucent plastic particles was placed at the bottom (see Fig. 3). In each experiment, we used one of two kinds of particles: almost cylindrical Poly(methyl methacrylate) (PMMA) particles with a typical length scale of 2–3 mm or spherical Polystyrene (PS) particles with a 580 μm diameter. For the heavier PMMA particles, salt was added to the water to reduce the relative density of the particles. For the two types of particles, the critical Shields parameter θ_{cr}

was estimated experimentally for the PMMA particles $\theta_{\mathrm{cr}} = 0.032 \pm 0.007$ and for the PS particles $\theta_{\mathrm{cr}} = 0.13 \pm 0.02$. An overview of the properties of the particles and the fluid is provided in Table I.

The rotating table was driven by a computer-controlled electric motor at the axle. An oscillating flow relative to the sediment bed is generated by making the table oscillate with an angular velocity $\Omega(t)$ given by Eq. (1). The amount of electric current that can be safely supplied to the motor is limited. Therefore, the torque and angular acceleration of the table are also limited. The highest angular acceleration that could be obtained was $(\partial \Omega/\partial t)_{\max} \approx 0.6$ rad s^{-2}. When forcing a sinusoidal motion of the form given by Eq. (1), the maximum angular acceleration is then $(\partial \Omega/\partial t)_{\max} = \Omega_o \omega < 0.6$ rad s^{-2}. As long as this limit is respected, the angular velocity of the table is controlled with a precision of 0.01 rad s^{-1}.

In the experiments discussed here, the values of the parameters are limited by the maximum acceleration of the table on one side and by the minimum shear stress (i.e., the critical Shields parameter) required to get particles into motion on the other. PMMA particles were used in 24 experiments with 0.6 rad/s $\leqslant \Omega_o \leqslant$ 1 rad/s and 0.01 Hz $\leqslant \omega/(2\pi) \leqslant$ 0.095 Hz. This means that for these experiments $35000 \lesssim \mathrm{Re} \lesssim 58000$, $0.09 \lesssim \mathrm{Sr} \lesssim 0.85$, and $12 \lesssim \Psi \lesssim 33$. It can be seen from the ranges of the Strouhal number that the critical value $\mathrm{Sr} = 0.64$ was barely reached for the PMMA particles. For this reason, we also performed the experiments with PS particles. These particles were used in 22 experiments with 0.17 rad/s $\leqslant \Omega_o \leqslant$ 0.6 rad/s and 0.02 Hz $\leqslant \omega/(2\pi) \leqslant$ 0.2 Hz, i.e., for $10\,000 \lesssim \mathrm{Re} \lesssim 36\,000$, $0.31 \lesssim \mathrm{Sr} \lesssim 7.39$, and, and $0.97 \lesssim \Psi \lesssim 12$. Most experiments lasted 5000 s ($\sim$1 h 23 min). Only three experiments with PMMA particles were performed for a longer time: one with a duration of 4.5 h, one with a duration of 5 h, and one with a duration of 8 h.

To contrast our findings with those of Stegner and Wesfreid [18], we also performed experiments in an annular

channel. For this, an extra cylinder with a 14.5 cm radius was placed in the center of the tank, leaving an annular region with a width of 10 cm. We performed additional experiments with PMMA particles in such geometry. Two had constant forcing parameters: Re = 37 500 and Sr = 0.63 and 0.85. One experiment had changing forcing parameters (see Sec. IV E for details). For each experiment in the annular geometry, there was an experiment performed in the cylindrical geometry with equivalent forcing.

Finally, we performed four experiments with PS particles with background rotation. For these experiments, the frequency was set to $\omega/(2\pi) = 0.08$ Hz. For three experiments, $\Omega_0 = 0.4$ rad s^{-1} with $\Omega_c = 0.05$, 0.1 and 0.2 rad s^{-1} so that Re = 24 000, Sr = 1.26, and Ro = 8, 4, and 2. For one experiment, $\Omega_0 = 0.3$ rad s^{-1} with $\Omega_c = 1.0$ rad s^{-1} so that Re = 18 000, Sr = 1.68, and Ro = 1.

B. Measurement technique

The sediment bed thickness was measured using a Light Attenuation Technique (LAT) based on the work by Munro and Dalziel [29]. This technique works by illuminating the sediment bed from below and capturing with a camera the amount of light transmitted through the bed. The light passing through the sediment experiences multiple reflections, refractions, and absorptions. The transmitted light intensity (I) can be related to the bed thickness through a calibration. The advantages of the LAT are a high temporal and spacial resolution, a relatively low cost, and a simple and fast post-processing algorithm. Some restrictions of this method are that the particles have to be transparent, the particle size distribution has to be narrow to avoid inhomogeneities in the attenuation, the maximum bed thickness is limited by the decay of the intensity with bed thickness, and particles in suspension have a negative impact on the accuracy.

To implement the LAT, a light bank consisting of eleven 18 W 615-mm-long TL bulbs separated 2.5 cm from each other was placed horizontally on the table, underneath the tank. A wooden plate that supports the tank contains a hole in the center such that the light can only enter through the cylinder's base. In addition, a 6-mm-thick white acrylic diffuser was placed in between the light bank and the tank, and a camera was placed above the center of the tank and fixed to the rotating table at a sufficient height to capture the full interior of the cylinder. The experiments with the PMMA particles were done with an Allied Vision Technologies 14 bit Pike F100-BC with a resolution of 1000×1000 pixels. This meant that one pixel in the image corresponds to 0.516×0.516 mm area. The experiments with the PS particles were performed with a Princeton Instruments MEGAPLUS ES2020 12bit grayscale camera with a resolution of 1600×1200 pixels. In this case, one pixel corresponds to 0.519×0.519 mm area. The cameras were connected to a co-rotating computer where the images were saved. The use of fluorescent tubes requires the exposure duration to be set to a multiple of 10 ms to match the mains electricity's AC half cycle. Otherwise, the exposure will not be the same for every frame.

A calibration is needed to convert light intensity into bed thickness. This calibration is carried out as follows. First, an image is taken with the tank filled with water but without

particles. The aperture and gain of the camera are set up such that this image is just saturated. In this way, we take advantage of the full dynamic range of the camera. Next, a flat particle layer of known thickness is deposited at the bottom of the tank, and another picture is taken. This is repeated for several layer thicknesses. For the PS particles, the thickness of the layers used was from 0 to 20 mm in 2.5-mm intervals. For the PMMA particles, the thickness of the layers was from 0 to 95 mm in 5-mm intervals. The choice of different layer thicknesses is due to the higher light absorption by the PS particles. For this reason, the initial thickness of the particle layer for the experiments with PMMA particles was set to 5 cm, while for experiments with PS particles, it was set to 2 cm.

For the calibration in the original method by Munro and Dalziel [29], they related the light intensity averaged over the whole plane to the average layer thickness. Our approach has to be somewhat different because of inhomogeneities in the illumination due to edges of the tank and the relative large size of the particles (particularly, the PMMA particles) compared to both a pixel and the changes in bed thickness. First, we removed the noise due to the particles by applying a Gaussian filter with standard deviation $\sigma = 10$ pixels. Afterwards, we fit for every pixel a function of the type:

$$\frac{I(z)}{I_0} = \exp(\alpha z^p), \qquad (12)$$

where I is the measured light intensity, I_0 is the light intensity for that pixel without any particles, and α and p are fitting parameters. Like Munro and Dalziel [29], we find this function to represent well the light decay as a function of the bed thickness. Finally, the bed thickness for every pixel $\mathbf{Z}$ is computed by inverting the previous function:

$$\mathbf{Z} = [\mathbf{A} - \mathbf{B}\ln(\mathbf{I})]^{\mathbf{C}}, \qquad (13)$$

where $\mathbf{I}$ is the two-dimensional matrix containing the light intensity captured by the camera, and $\mathbf{A}$, $\mathbf{B}$, and $\mathbf{C}$ are matrices containing the fitting parameters for every pixel ij: $A_{ij} = \ln(I_{0ij})/\alpha_{ij}$, $B_{ij} = 1/\alpha_{ij}$, and $C_{ij} = 1/p_{ij}$.

To test the calibration, we reconstructed flat particle beds of different thickness. Again, we first smoothed the image by applying a Gaussian filter with $\sigma = 10$ pixels. Then, we applied the function Eq. (13). For the PMMA particles, the spatial variations in the bed were about $\pm 2d$, and the average error over the whole plane was about 3 mm, which is approximately one particle. For the PS particles, the spatial variation are in the order of 2.5 mm (about $\pm 5d$), and the average error over the whole plane was about 1.5 mm (about $\pm 3d$). However, large amounts of particles were suspended in several experiments (i.e., mainly for large Re values) that generated an additional inhomogeneous error in the measurements. After the analysis of the experiments, we estimate that the error could reach up to 10–12 mm for the experiments with PMMA particles and up to 6–7 mm for experiments with the PS particles. This prevented us from computing satisfactorily quantities related, for example, to the net radial transport, but this had no impact in the measurements of the ripple wavelength (i.e., our main interest).
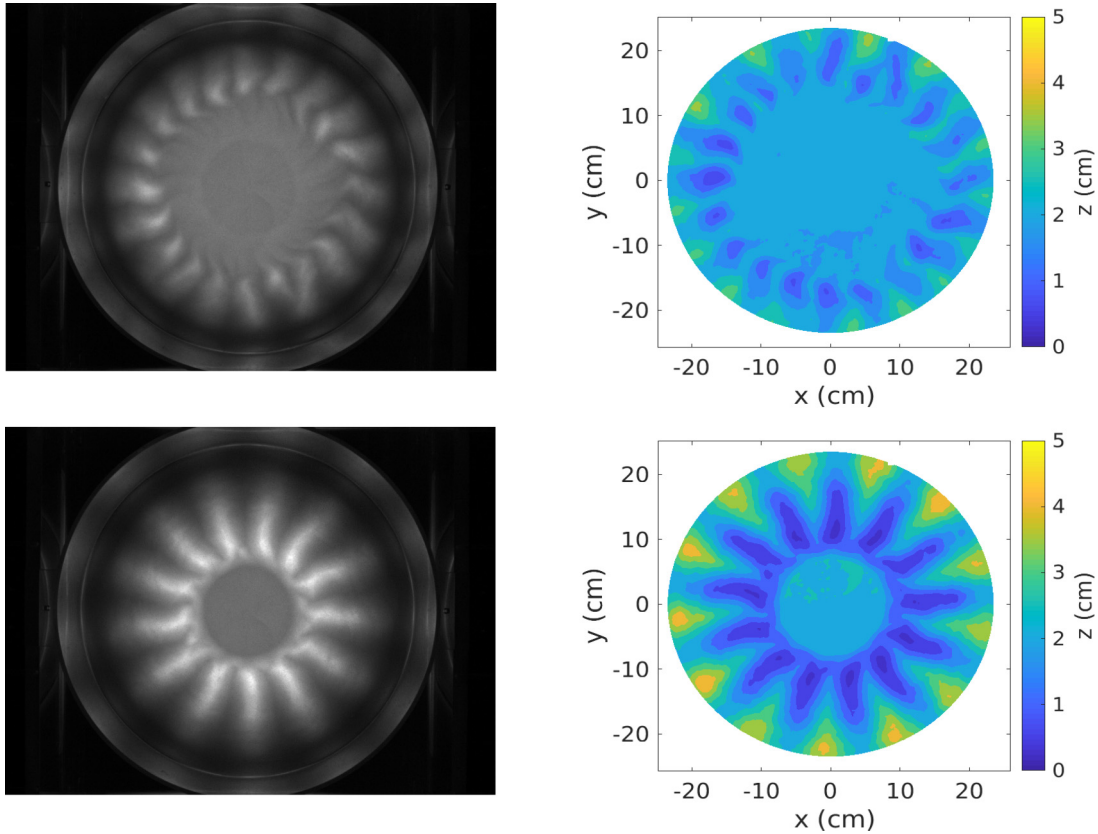
FIG. 4. Raw images (left) and reconstructed bed thicknes (right) for an experiment with PS particles, Re = 24 000, Sr = 2.20, and Ro = ∞ at two different times $t = 250$ s (top) and $t = 5000$ s (bottom).

IV. RESULTS AND DISCUSSION

A. Pattern and ripple formation

Typical patterns observed in the experiments are shown in Fig. 4 using both the raw images and the reconstructed sediment thickness at two different times for an experiment with PS particles, Re = 24 000, Sr = 2.20, and Ro = ∞. When the table starts to oscillate, short radial ripples start forming at the outer edge of the tank. Then, these ripples grow toward the center of the tank while, at the same time, merging to create coarser ripples. After reaching a quasisteady situation, the radial ripples extend from the outer wall up to an area where the bed remains undisturbed because the flow velocities there are not large enough to make the particles move. This general result is in agreement with Rousseaux *et al.* [19]. Clearly, the extent of the undisturbed area depends on the forcing parameters up to the point that it completely vanishes for the experiments with PMMA particles and the largest Re values.

The coarsening process can also be observed in Fig. 5 where we show the bed elevation as a function of time for a circular cross section near the outer wall (at $r = 23$ cm). Next to it, we plot its Fourier transform as a function of time together with the number of ripples detected by counting the number of crests and troughs. Initially, there is a rapid coarsening process that lasts about 1000 s. For the experiment shown in Fig. 5, it lasts about 500 s until the number of ripples reaches a quasisteady situation with 14 ripples that remain until a last merger at $t \approx 3500$ s. In general, there is a good

agreement between the largest peak in the Fourier transform and the number of ripples counted. However, close to merger events, the largest peak in the Fourier transform is blurred, signaling the coexistence of two modes.

B. Effect of curvature on radial transport and the critical radius

Following the discussion in Sec. II, the most direct way to observe the effect of curvature (i.e., of the Strouhal number Sr) when Ro = ∞ is to study the radial transport, since the radial shear stress pulsates in the outward direction, and its magnitude depends on the Sr value. We consider the experiments with PS particles and Re = 24 000 since the Sr values of these experiments span through the transition value Sr = 0.64. Experiments with only one Re value are used because otherwise the total shear stress and the total amount of sediment transported varies greatly. Hence, this is a fairer comparison.

The difference in height of the sediment bed with respect to the initial height for the two extreme experiments [Sr = 2.20 shown in Fig. 4(d) and Sr = 0.31 shown in Fig. 6] clearly demonstrates that more sediment is transported toward the cylinder wall for the smaller Sr value. Instead of only an oscillating pattern in the azimuthal direction like for Sr = 2.20, we can observe a half ring with larger bed thickness close to the outer boundary for Sr = 0.31. This confirms that the domain's curvature has an effect for small Sr values.
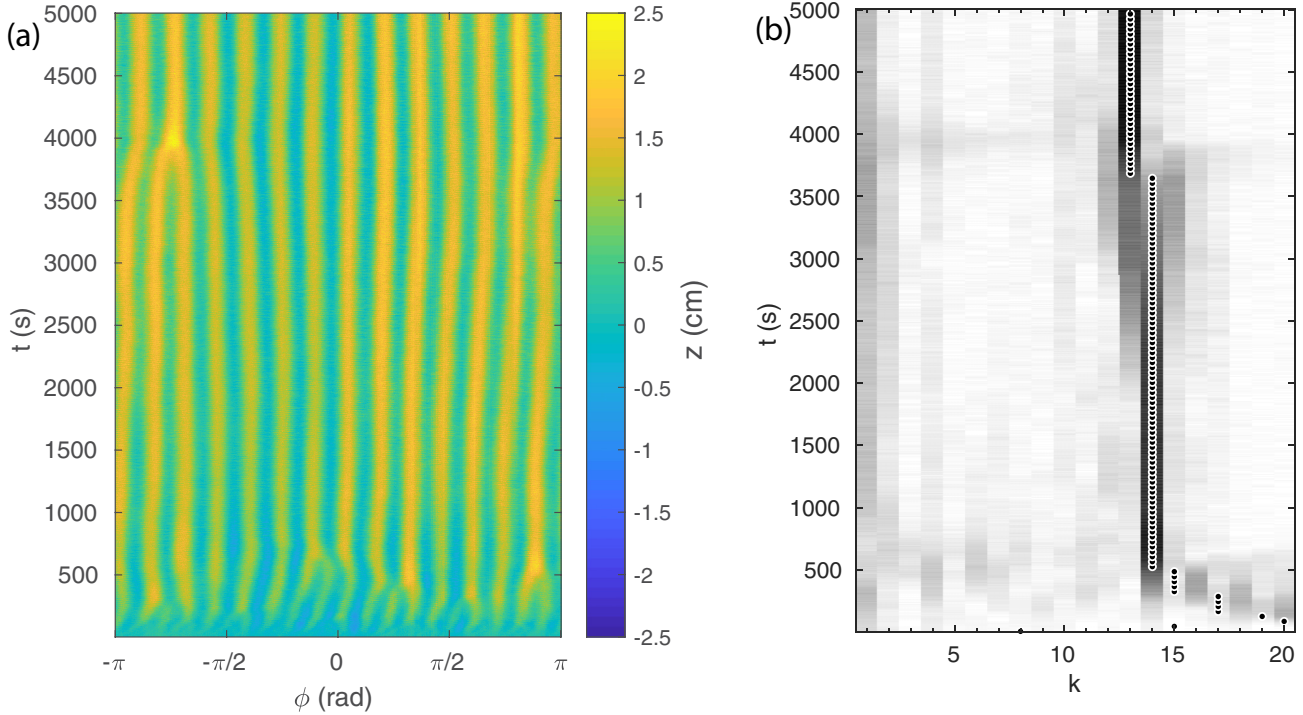
FIG. 5. Example of the evolution of the number of ripples as a function of time at a cross-section at $r = 0.23$ cm. (a) Changes in bed elevation as a function of time. (b) Fourier transform for every cross section of the bed elevation (gray-scale) and number of ripples (black-and-white bullets). Results are from the experiment with PS particles, Re = 24 000, Sr = 2.20, and Ro = ∞.

Another effect of the domain's curvature is observed in the extent of the undisturbed region at the center of the tank. To demonstrate this, we consider the radius R_c of a circle fitted to the undisturbed region, and we define the maximum shear stress for a Stokes boundary layer at this radius as

$$\tau_{st}(r = R_c) = R_c \rho_l \nu^{1/2} \Omega_o^{3/2} Sr^{1/2}. \tag{14}$$

Figure 7 shows this stress $\tau_{st}(r = R_c)$, normalized with the critical shear stress needed to get the particles in motion τ_c, as a function of Sr. If τ_{st} was not normalized by the critical

shear stress, the results for the two types of particles would be far apart. It is this normalization that causes the results to come together. For large values of the Strouhal number, it appears that $\tau_{st}(r = R_c) \approx \tau_c$, meaning that the erosion can all be explained by the Stokes boundary layer. As the Strouhal number decreases, $\tau_{st}(r = R_c)/\tau_c$ decreases, meaning that the
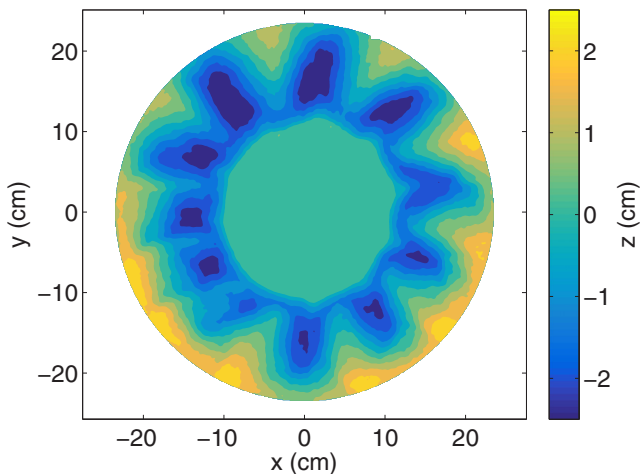

FIG. 6. Changes in sediment bed thickness between $t = 0$ and $t = 5000$ s for the experiments with PS particles, Re = 24 000, Sr = 0.31, and Ro = ∞.
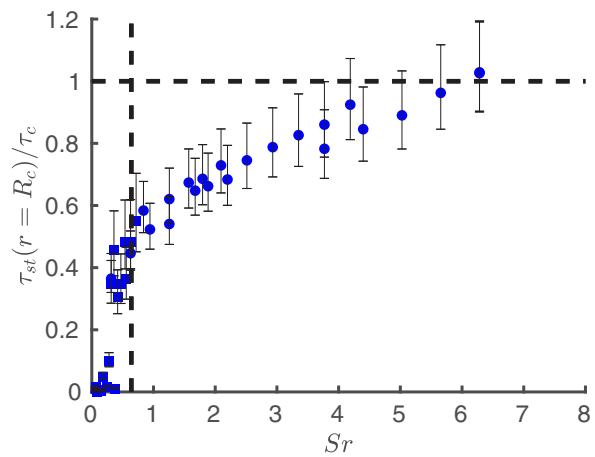

FIG. 7. Shear stress for a Stokes boundary layer at the critical radius R_c [see Eq. (14)] normalized with the critical shear stress for sediment motion τ_c as a function of the Strouhal number. Squares denote the experiments with PMMA particles and bullets those with PS particles. The error bars denote the error in determining the critical shear stress. The horizontal dashed line represents $\tau_{st}(r = R_c)/\tau_c = 1$ and the vertical dashed line represents Sr = 0.64.
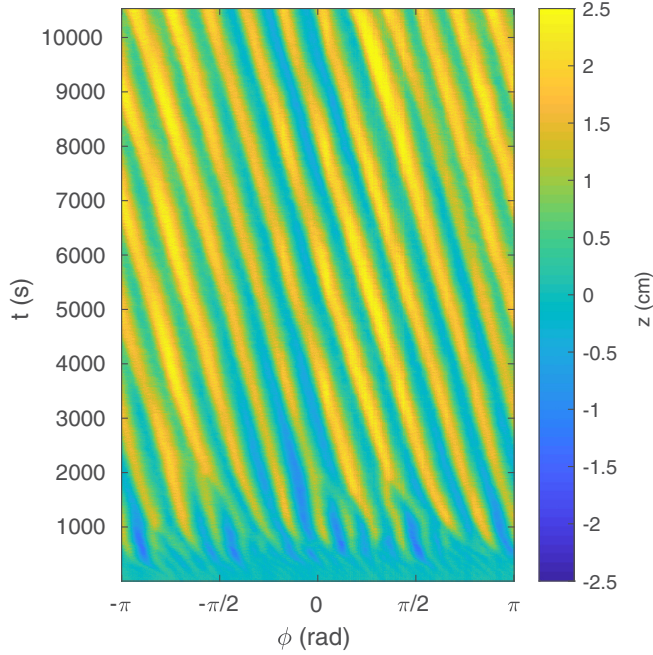
FIG. 8. Changes in the bed elevation as a function of time and angular position at a cross-section at $r = 0.23$ cm for an experiment with PS particles with Re $= 37\,500$, Sr $= 1.26$, and Ro $= 2$.

shear stress provided by a Stokes boundary layer at $r = R_c$ is in principle not large enough to get particles eroded. There must be an additional contribution from the radial component that grows in magnitude and gets more synchronized with the azimuthal component. This creates radial transport and a steep slope right outside $r = R_c$ that facilitates the motion of the sediment grains. Finally, there is a clear change in the slope of the curve in Fig. 7 at the critical value for Sr $= 0.64$ (indicated by the vertical broken line) when the curvature of the domain starts to dominate. This supports our claim that the secondary motion has an effect on the final bed morphology.

C. Effect of background rotation on pattern and ripple formation

When background rotation is added, the formation of the ripples begins at the outer edge, as in the case without background rotation. Several small ripples form, and a coarsening process starts until a final number of ripples is reached. However, as can be seen in Fig. 8, the ripples propagate azimuthally when background rotation is present. This is explained by the asymmetry in the velocity due to the preferential rotation direction, as discussed in Sec. II B. The propagation speed depends then on the magnitude of the background rotation.

Additionally, it can be seen from the final patterns shown in Fig. 9 that the ripples are oblique instead of radial. For the two cases with weaker background rotation [Ro $= 8$ and Ro $= 4$, shown in Figs. 9(a) and 9(b)], the ripples have a uniform positive angle with respect to the radial direction. This is explained by the fact that the flow due to the secondary motion oscillates from radially inward to radially outward in the Ekman boundary layer due to the Coriolis force. Superimposing this to the primary azimuthal motion results in a flow near

the bed that oscillates in a direction oblique to the azimuthal direction.

For the experiments with the strongest background rotation [Figs. 9(c) and 9(d)], the angle of the ripples with respect to the radial direction is not homogeneous. This is particularly clear for the experiment with Ro $= 1$ [Fig. 9(d)]. For this experiment, the final pattern can be divided into three regions. At the center (for $r \lesssim 5$ cm), there is the undisturbed area. For 5 cm $\lesssim r \lesssim 15$ cm, there is a region with ripples oriented with a positive angle with respect to the radial direction. For $r \gtrsim 15$ cm, the ripples are oriented with a negative angle with respect to the radial direction. A possible reason for these different zones is that the flow is only strong enough to move the sediment in both directions in the outermost region due to the large asymmetry in the shear stress between the cyclonic and the anticyclonic part of the oscillation. In the middle region, no large ripples form because the particles are only transported in one direction, and there is a strong radially outward transport since the largest shear stress occurs during the anticyclonic part of the oscillation for which the radial flow is outward. It is important to note that the inner and outer regions seem to be somewhat decoupled in that there is not necessarily a correspondence ripple by ripple. In fact, for the experiment with Ro $= 2$ [Fig. 9(d)], there are 10 ripples in the inner region and 11 in the outer region. Clearly, the ripple wavelength does not necessarily vary linearly with r, and hence, cannot be simply explained as being proportional to the excursion length of the primary motion as defined in Eq. (2).

D. Ripple wavelength selection

The most common question about sand ripples is the dependence of their geometry, and in particular, the wavelength λ on the parameters of the problem. To answer this question, we counted the number of ripples k at the end of all experiments ($t = 5000$ s), as in Fig. 5(b), and computed the wavelength $\lambda = 2\pi r/k$.

The first important result is that the wavelength does not depend exclusively on the excursion length. Instead, we find that the wavelength depends on Re$_L$. This can be seen in Fig. 10 where we show a log-log plot of the normalized wavelength λ/R as a function of Re$_L$. In this plot most of the data points collapse into a line within an error of one ripple. We chose the error bars at ± 1 ripple because we are treating the wavelength as a continuous variable while in reality it can only have discrete values. Clear exceptions of the data collapse are observed for experiments with PS particles and low values of the bed shear stress parameter T (dark bullets) for which the shear stress is barely larger than the estimated critical shear stress. These exceptions may be due to the slower development of the ripples so that 5000 s are not enough to reach the final configuration or are still rolling-grain ripples instead of vortex ripples. A fit excluding these exceptions (experiments with $T < 0.2$) suggests that $\lambda/R \propto$ Re$_L^{0.42\pm0.02}$. Furthermore, the seamless transition between the experiments with PS and PMMA particles suggests that the sediment properties do not play a role in determining the ripple wavelength, in agreement with classical results [23].

To compare our results with the "2/3-law" and the results of Stegner and Wesfreid [18] in an annular geometry, we plot
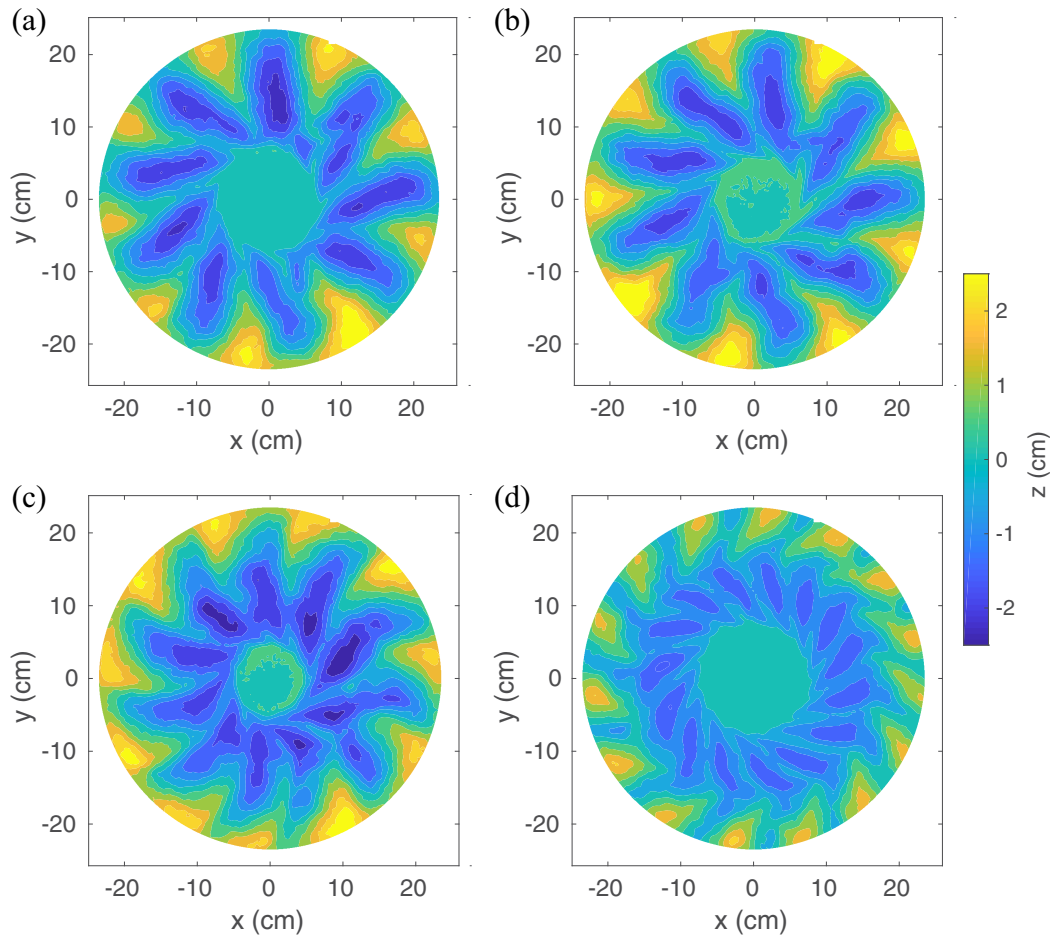
FIG. 9. Changes in sediment bed thickness between $t = 0$ and $t = 5000$ s for the experiments with background rotation. All experiments were done with PS particles. The values of the nondimensional parameters are (a) Ro = 8, (b) Ro = 4, (c) Ro = 2, with Re = 24 000 and Sr = 1.26, and (d) Ro = 1, with Re = 18 000 and Sr = 1.7.

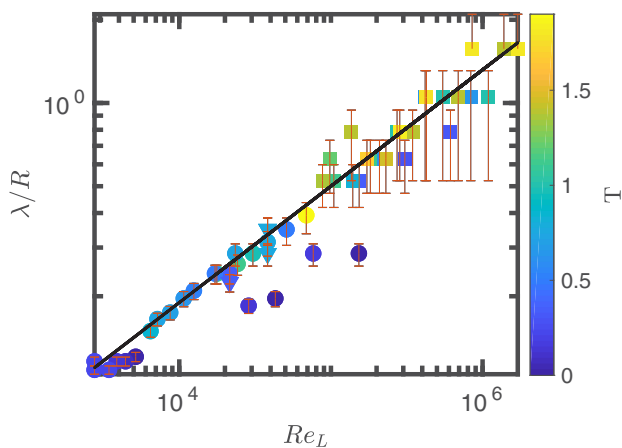FIG. 10. Ripple wavelength λ normalized with the radius R as a function of Re_L. The experiments with PMMA particles are denoted by squares, and the experiments with PS particles by bullets. The triangles denote experiments with PS particles and background rotation. The error bars denote the wavelength plus or minus one ripple. The color denotes the bed shear stress parameter given by Eq. (8).
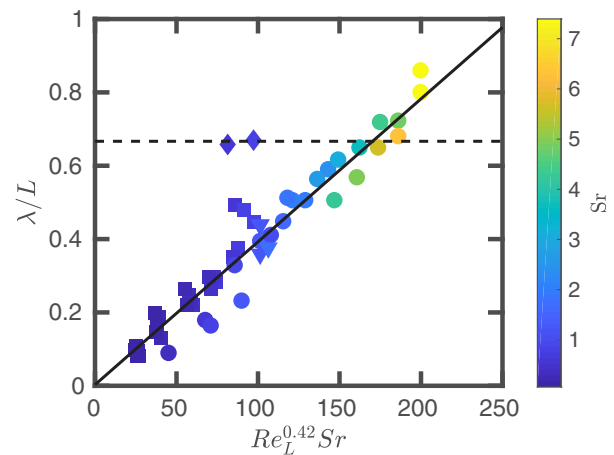
FIG. 11. Ripple wavelength λ normalized with the excursion length L as a function of $Re_L^{0.42}$Sr. The experiments with PMMA particles are denoted by squares, and the experiments with PS particles by bullets. The diamond symbols correspond to experiments with PMMA particles in an annular configuration. The triangles correspond to experiments with PS particles and background rotation. The marker's color denotes the Strouhal number Sr. The dashed line denotes the "2/3-law."
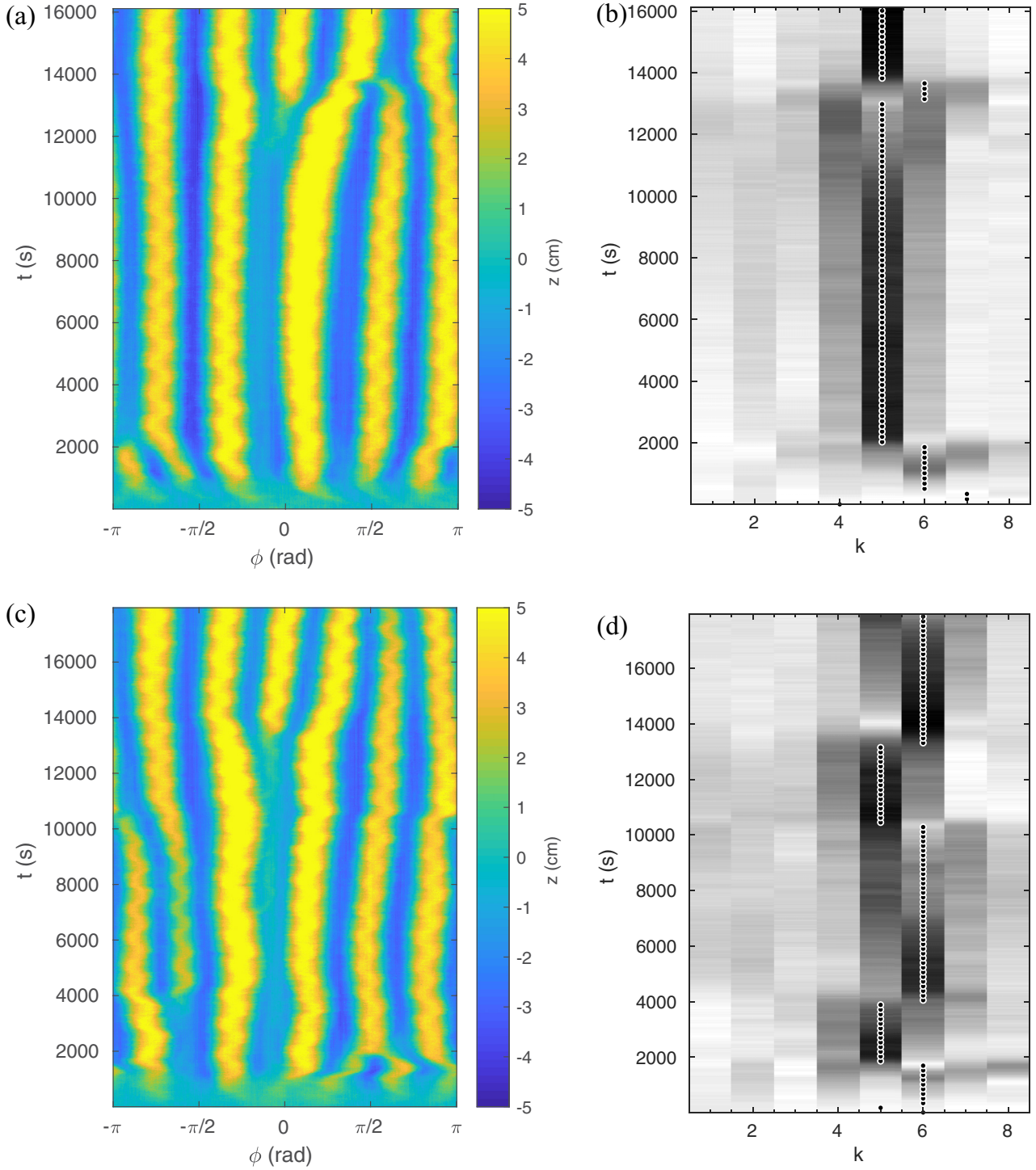
FIG. 12. Evolution of the number of ripples as a function of time at a cross-section at $r = 0.23$ cm for one 4.5-h-long experiment and for one 5-h-long experiment both with PMMA particles. Upper row: Re = 37 500, Sr = 0.76. Lower row: Re = 37 500, Sr = 0.85. Left column: Changes in the bed elevation. Right column: Fourier transform of the bed thickness (gray scale) and number of ripples counted (black-and-white bullets).

the wavelength λ normalized with the excursion length L at $r = 0.23$ cm as a function of $\mathrm{Re}_L^{0.42}\mathrm{Sr}$ (Fig. 11). A linear fit suggests that

$$\frac{\lambda}{L} \approx (4.0 \pm 0.2)10^{-3}\, \mathrm{Re}_L^{0.42}\mathrm{Sr}. \qquad (15)$$

This result clearly differs from the "2/3-law" that states that $\lambda/L = 2/3$. To check that the difference is not due to differences in the sediment characteristics or the values of the control parameter, we also performed two experiments with PMMA particles and an annular configuration (as explained in Sec. III). For these two experiments, the radius of the inner
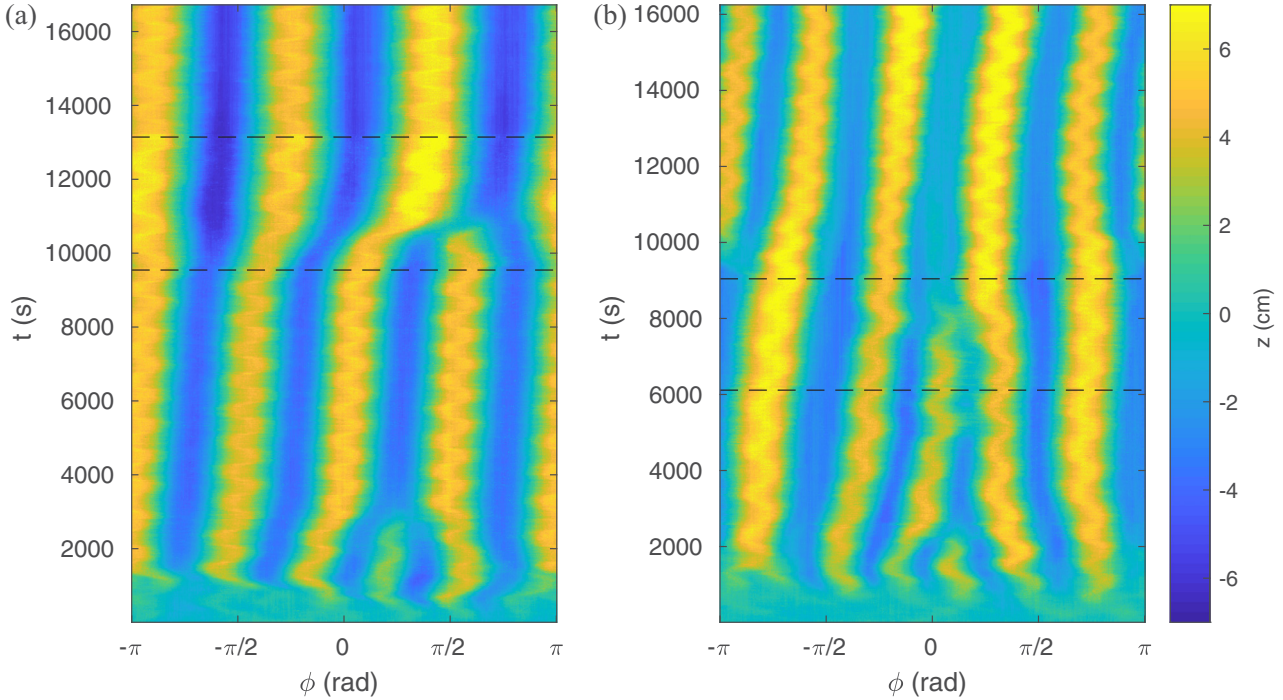
FIG. 13. Difference in the bed elevation as a function of time and angular position at a cross-section at $r = 0.23$ cm for two experiments with forcing changing conditions in an (a) annular configuration and (b) a cylindrical configuration. Both experiments were carried out with PMMA particles. Initially Re = 37500 and Sr = 0.63. During the period in between the dashed lines, Sr is set to Sr = 0.85. After this period, the value of Sr is returned to its original value.

cylinder was larger than the critical radius for particle motion. As can be seen in Fig. 11 (diamonds), for these experiments $\lambda/L \approx 2/3$, implying that the difference is indeed due to the geometry.

From all the experiments performed, those with the highest value of Sr are the closest to the intersection between the relationship given in Eq. (15) and the relationship $\lambda/L = 2/3$, that occurs for $\mathrm{Re}_L^{0.42}\mathrm{Sr} \approx 170$. These Sr values are much larger than the critical value Sr = 0.64 discussed in Sec. II B. In fact, there is no clear transition or distinction in the relationship between the wavelength and the problem parameters for experiments with Sr < 0.64 and Sr > 0.64.

Earlier work by Rousseaux *et al.* [16] in a cylinder with different dimensions and using different sediment suggested that the "2/3-law" also applied to vortex ripples in a cylindrical domain or at least that $\lambda \propto L$. When reviewing some of their experiments, for example, those shown in Figs. 1(d) and 7(b) of their paper, we find that values of $\mathrm{Re}_L^{0.42}\mathrm{Sr}$ are equal to 184 and 227 which are close to the intersection occurring at $\mathrm{Re}_L^{0.42}\mathrm{Sr} \approx 170$. This indicates a good agreement with the results presented in the current paper and suggests that the fact that $\lambda/L \approx 2/3$ for those experiments is probably a coincidence.

Unfortunately, the technical limitations of our experimental setup did not allow us to perform experiments for values of $\mathrm{Re}_L^{0.42}\mathrm{Sr} \gg 170$. Hence, we could not check if there is a trend toward an asymptote close to $\lambda/L = 2/3$. However, the two experiments with $\mathrm{Re}_L^{0.42}\mathrm{Sr} = 206$ suggest that the relationship given by Eq. (15) still holds.

E. Pattern stability

In this section, we present results on the long-term stability and evolution of the number of ripples for two 5-h-long experiments and for one experiment with changing forcing conditions. The motivation for these experiments is twofold: (1) we would like to know if counting the number of ripples after 5000 s (the duration of most experiments) is representative of the final number of ripples, and (2) we would like to know if there is hysteresis in the coarsening/splitting process of the ripples, as found by Stegner and Wesfreid [18] in an annular geometry.

For experiments with low value of the bed-shear parameter T ($T < 0.2$), the bed and the number of ripples were still changing after 5000 s. However, for most experiments with larger T values, the number of ripples seemed to have reached a constant value, as in Fig. 5. Even then, for our previous analysis we considered the possibility of making an error of one ripple. For the long experiments, we used PMMA particles with Re = 37 500 and Sr = 0.76 and 0.85. The difference in Sr is small because we were interested to see what happens when this parameter and the number of ripples are slightly perturbed. This change in Sr would be equivalent to a difference of about 0.3 ripples, which is in principle not possible because there must be an integer number of ripples. The resulting evolution of the bed elevation at $r = 0.23$ cm and the number of ripples is shown in Fig. 12. For the experiment with Sr = 0.76, the number of ripples reaches five at about 2000 s and remains quite constant afterwards, except for a short period of time at around $t = 13\,000$ s where it jumps to six. This is

already surprising in the light of the results by Stegner and Wesfreid [18] in an annular geometry who found that an increase of the number of ripples was not possible even when changing the forcing conditions. For the experiment with Sr = 0.85, the changes are more dramatic. After reaching again a configuration with five ripples at $t \approx 2000$ s, it switches to six ripples for over 6000 s then back to five and back to six. This shows that (1) in a cylindrical domain it is possible for the number of ripples to grow (i.e., there is no hysteresis), and (2) that the stability of the number of ripples depends also on the value of the governing parameters. The number of ripples will probably be more stable as it is closer to a governing parameter combination associated to an integer number of ripples. However, Eq. (15) is not suitable to determine such a combination because it treats the wavelength as a continuous variable.

To further check the lack of hysteresis, we performed two experiments with changing forcing conditions. One experiment was performed in the cylindrical tank and one in the annular tank. In both cases, PMMA particles were used, Re = 37 500, and initially, the value of Sr was set to Sr = 0.63. The bed evolution at $r = 23$ cm for these experiments is shown in Fig. 13. When reaching a steady state under these conditions, four ripples were observed in the cylindrical tank and five ripples in the annular tank. Afterwards, the value of Sr was changed to Sr = 0.85 for about 3000 s by decreasing the frequency of oscillation. During this period, the number of ripples decreased by one for both experiments. Then, the value of Sr was returned to Sr = 0.63. For the experiment in the annular tank, the number of ripples remained constant, while for the cylindrical tank, the number of ripples increase by one again. This confirms that the there is no hysteresis in a cylindrical tank, implying that the number of ripples can increase or decrease when changing the forcing conditions.

inside a cylinder with and without the addition of background rotation. Experiments in this geometrical configuration have been used in the past as attempts to understand the evolution of vortex ripples in straight wave flumes [1,16]. However, we have shown that the evolution of vortex ripples under an oscillating flow inside a cylinder differs greatly with that inside straight flumes or annular containers. In particular, the ripple wavelength normalized with the excursion length in a cylindrical container depends on both the Reynolds number and the Strouhal number instead of being constant. This can be attributed to the secondary circulation that contributes an additional radial velocity at the bottom and arises due to the curvature of the container. The addition of background rotation modifies the secondary motion and alters the vortex ripples by changing their orientation and forcing them to migrate azimuthally.

Ripples in an oscillating cylindrical container exhibit a highly dynamic behavior: the number of ripples changes back and forth even when the forcing parameters are kept constant. This differs from the results in experiment in annular geometries for which there is hysteresis in the sense that the number of ripples can decrease but not increase when the forcing is changed. This is probably explained by the fact that several processes in the evolution of vortex ripples are three-dimensional [30] and might be suppressed if the distance between the two walls of the flume are too close together. In an annular channel, the three-dimensionality due to the radial dependence of the ripples should emerge as the radius of the inner cylinder becomes smaller than the critical radius for sediment motion. In an oscillating cylinder, ripples are by definition three-dimensional. In this way, the evolution of vortex ripples in a cylindrical domain is of interest for the fundamental study of the interaction of bedforms and an oscillating flow even if this evolution differs from the classical quasi-two-dimensional picture in a straight flume or under waves.

V. CONCLUSIONS

We present results of laboratory experiments on the evolution and geometry of vortex ripples under an oscillating flow

ACKNOWLEDGMENTS

[1] C. de Candolle, Arch. Sci. Phys. Nat. **3**, 253 (1882).

[2] G. H. Darwin, P. R. Soc. London **36**, 18 (1883).

[3] F. Pedocchi and M. H. García, J. Geophys. Res.-Oceans **114**, C12014 (2009).

[4] R. L. Soulsby, R. J. S. Whitehouse, and K. V. Marten, Cont. Shelf Res. **38**, 47 (2012).

[5] T. R. Nelson, G. Voulgaris, and P. Traykovski, J. Geophys. Res.-Oceans **118**, 3202 (2013).

[6] A. M. Penko, J. Calantoni, S. Rodriguez-Abudo, D. L. Foster, and D. N. Slinn, J. Geophys. Res.-Oceans **118**, 1543 (2013).

[7] A. G. Kidanemariam and M. Uhlmann, J. Fluid Mech. **750**, R2 (2014).

[8] J. R. Finn, M. Li, and S. V. Apte, J. Fluid Mech. **796**, 340 (2016).

[9] K. Lofquist, Sand ripple growth in an oscillatory-flow water tunnel, Tech. Rep. Tech. Paper No. 78-5 (U.S. Army Corps of Engineers, Coastal Engr. Res. Center, 1978).

[10] T. O'Donoghue and G. S. Clubb, Coast. Eng. **44**, 101 (2001).

[11] T. O'Donoghue, J. S. Doucette, J. J. van der Werf, and J. S. Ribberink, Coast. Eng. **53**, 997 (2006).

[12] F. Pedocchi and M. H. García, J. Geophys. Res.-Oceans **114**, C12015 (2009).

[13] F. Y. Testik, S. I. Voropayev, and H. J. S. Fernando, Phys. Fluids **17**, 072104 (2005).

[14] G. Ruessink, J. A. Brinkkemper, and M. G. Kleinhans, J. Mar Sci. Eng. **3**, 1568 (2015).

[15] G. Rousseaux, A. Stegner, and J. E. Wesfreid, Phys. Rev. E **69**, 031307 (2004).

[16] G. Rousseaux, J. Kruithof, P. Jenffer, and J. E. Wesfreid, Phys. Rev. E **78**, 016302 (2008).

[17] M. A. Scherer, F. Melo, and M. Marder, Phys. Fluids **11**, 58 (1999).

[18] A. Stegner and J. E. Wesfreid, Phys. Rev. E **60**, R3487 (1999).

[19] G. Rousseaux, H. Caps, and J. E. Wesfreid, Eur. Phys. J. E **13**, 213 (2004).

[20] J. J. Williams, P. S. Bell, P. D. Thorne, N. Metje, and L. E. Coates, J. Geophys. Res.-Oceans **109**, C02004 (2004).

[21] M. C. Miller and P. D. Komar, J. Sediment. Res. **50**, 183 (1980).

[22] P. L. Wiberg and C. K. Harris, J. Geophys. Res.-Oceans **99**, 775 (1994).

[23] R. A. Bagnold and G. I. Taylor, Proc. R. Soc. London, Ser. A **187**, 1 (1946).

[24] M. S. Longuet-Higgins, J. Fluid Mech. **107**, 1 (1981).

[25] J. H. Nienhuis, J. T. Perron, J. C. T. Kao, and P. M. Myrow, J. Geophys. Res.-Earth **119**, 2239 (2014).

[26] J. M. Owen and R. H. Rogers, *Flow and Heat Transfer in Rotating Disc Systems*, Vol. 1: Rotor-Stator Systems (Research Studies Press, London, 1989).

[27] L. C. Van Rijn, *Principles of Sediment Transport in Rivers, Estuaries, and Coastal Seas* (Aqua Publications, Amsterdam, 1993).

[28] P. Nielsen, J. Geophys. Res. **86**, 6467 (1981).

[29] R. J. Munro and S. B. Dalziel, Exp. Fluids **39**, 602 (2005).

[30] J. L. Hansen, M. van Hecke, A. Haaning, C. Ellegaard, K. H. Andersen, T. Bohr, and T. Sams, Nature **410**, 324 (2001).